# Force Field for Mg^{2+}, Mn^{2+}, Zn^{2+}, and Cd^{2+} Ions That Have Balanced Interactions with Nucleic Acids

Maria T. Panteva, George M. Giambaşu, and Darrin M. York*

Center for Integrative Proteomics Research, BioMaPS Institute and Department of Chemistry & Chemical Biology, Rutgers University, 174 Frelinghuysen Road, Piscataway, New Jersey 08854-8076, United States

Ⓢ Supporting Information

ABSTRACT: Divalent metal ions are of fundamental importance to the function and folding of nucleic acids. Divalent metal ion−nucleic acid interactions are complex in nature and include both territorial and site specific binding. Commonly employed nonbonded divalent ion models, however, are often parametrized against bulk ion properties and are subsequently utilized in biomolecular simulations without considering any data related to interactions at specific nucleic acid sites. Previously, we assessed the ability of 17 different nonbonded Mg^{2+} ion models to reproduce different properties of Mg^{2+} in aqueous solution including radial distribution functions, solvation free energies, water exchange rates, and translational diffusion coefficients. In the present work, we depart from the recently developed 12−6−4 potential models for divalent metal ions developed by Li and Merz and tune the pairwise parameters for Mg^{2+}, Mn^{2+}, Zn^{2+}, and Cd^{2+} binding dimethyl phosphate, adenosine, and guanosine in order to reproduce experimental site specific binding free energies derived from potentiometric pH titration data. We further apply these parameters to investigate a metal ion migration previously proposed to occur during the catalytic reaction of the hammerhead ribozyme. The new parameters are shown to be accurate and balanced for nucleic acid binding in comparison with available experimental data and provide an important tool for molecular dynamics and free energy simulations of nucleic acids where these ions may exhibit different binding modes.
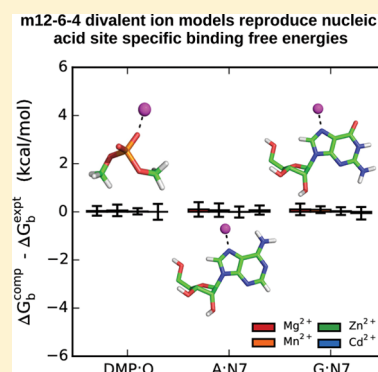
INTRODUCTION

The importance of divalent metal ions for RNA structure and function is crucial. Divalent metal ions, and in particular Mg^{2+}, not only drive nucleic acid folding[1,2] but also provide necessary structural stability in folded RNA and DNA structures by screening the negatively charged phosphate backbone through electrostatic interactions.[3,4] Divalent metal ions have even been found to play direct roles in reactions catalyzed by certain ribozymes.[5,6] In this study, we focus our attention on four specific divalent metal ions—Mg^{2+}, Mn^{2+}, Zn^{2+}, and Cd^{2+}—due to their important roles in RNA biochemistry as well as their different physicochemical properties. There are various examples of RNA structures that exhibit binding of these cations, including binding of Mn^{2+} and Zn^{2+},[7] multiple Mg^{2+} "cofactors",[8] and even 11 different divalent cations bound to RNA duplexes.[9] Further, certain riboswitches are known to bind a select group of divalent cations specifically.[10] Mg^{2+} is also believed to be directly involved in the catalytic reaction of the hepatitis delta virus ribozyme,[11−13] while both Mn^{2+} and Cd^{2+} have proven instrumental in thio-effect experiments to probe the catalytic mechanism.[14−17]

The ubiquitous presence of these cations in RNA biochemistry[18−20] has thus warranted the development of divalent ion models for use in biomolecular simulations. Typically, these models are parametrized against experimental bulk properties of the ion such as the ion solvation free energy, ion−water first shell equilibrium distance, radial distribution function, ion−water exchange rate,[21−25] or, in some cases, directly against quantum mechanical structural and energetic data.[26−28] Further, divalent ion models have been parametrized for use in various types of force fields including conventional molecular mechanical[26,29−38] and polarizable[39−46] models.

Polarizable force fields include many-body quantum effects that provide a more rigorous physical framework for modeling molecular interactions but are also more computationally intensive than their nonpolarizable counterparts. Currently, by far the most common and mature force fields applied in simulations of nucleic acids are of the nonpolarizable form, and consequently ion models that can be used consistently with these force fields are the focus of the present work.

Previously, we evaluated 17 different nonpolarizable nonbonded Mg^{2+} ion models in their ability to reproduce multiple bulk ion properties including equilibrium ion−water distances, ion hydration free energies, water exchange rates, and ion diffusion coefficients,[47] with the ultimate goal of developing more balanced divalent ion models that can provide a predictive understanding of the ion atmosphere around RNA. We showed that a group of water model-dependent Mg^{2+} models, based on a "12−6−4" potential,[24] were the only models capable of simultaneously reproducing multiple bulk properties of

magnesium. In the present work, we depart from the 12−6−4 models for four divalent metal ions important in RNA biochemistry, Mg^{2+}, Mn^{2+}, Zn^{2+}, and Cd^{2+}, assess their interactions with specific nucleic acid sites and reparametrize them to be more balanced in terms of their interaction with RNA relative to water. Specifically, we have tuned pairwise parameters for these four cations and the N7 atom of guanosine and adenosine and the nonbridging phosphate oxygen of dimethyl phosphate (DMP) to reproduce the experimental site specific binding free energies obtained from potentiometric pH titration binding affinity data.[48] Our results show that the original 12−6−4 parameters generally overestimate the interaction with the phosphodiester group and underestimate the interaction with the N7 of the purine residues by several kcal/mol. Our new parameters, the so-called m12−6−4 models, reduce the average error in the computed binding free energies to be within 0.1 kcal/mol of experiment. We further apply both the original and new parameter sets to investigate a metal ion migration hypothesized to occur during the hammerhead ribozyme catalytic mechanism.[49] The free energy barriers obtained for metal ion migration suggest that a divalent metal ion is generally more likely to be found in the crystallographic binding site in the reactant state when employing the m12−6−4 parameters compared to the 12−6−4 ion models, although all free energy profiles are characterized by a global energy minimum at a second ion binding site.

■ METHODS

All simulations were carried out using the AMBER14[29] molecular dynamics package, the ff14SB force field, and the TIP4PEw[50] water model (unless otherwise specified in the text). Dimethyl phosphate parameters were taken from Dupradeau et al.[51]

Pairwise Potential Functions. The potential functional form for the 12−6−4 ion parameters consists of both electrostatic and van der Waals interactions. The former is modeled using Coulomb pair potentials, $q_i q_j/r_{ij}$, where i and j represent two particles, q_i and q_j are the charges belonging to the particles, and r_{ij} is the distance between the particles. The latter expands upon the classic Lennard-Jones (12−6) potential by including an extra attractive term that falls off as r^{-4}, denoted as a 12−6−4 potential. Both the 12−6 and 12−6−4 potentials are described below.

The 12−6 potential[52] for nonbonded interactions is

$$U_{ij}(r_{ij}) = \varepsilon_{ij}\left[\left(\frac{R_{ij}}{r_{ij}}\right)^{12} - 2\left(\frac{R_{ij}}{r_{ij}}\right)^{6}\right] \tag{1}$$

where R_{ij} and ε_{ij} are the pairwise parameters equal to the combined radius and well depth, respectively, and r_{ij} is the particle separation distance. Equation 1 can be equivalently written as

$$U_{ij}(r_{ij}) = \frac{A_{ij}}{r_{ij}^{12}} - \frac{B_{ij}}{r_{ij}^{6}} \tag{2}$$

where $A_{ij} = \varepsilon_{ij}R_{ij}^{12}$ and $B_{ij} = 2\varepsilon_{ij}R_{ij}^{6}$.

The expanded 12−6−4 potential[24] is then

$$U_{ij}(r_{ij}) = \varepsilon_{ij}\left[\left(\frac{R_{ij}}{r_{ij}}\right)^{12} - 2\left(\frac{R_{ij}}{r_{ij}}\right)^{6} - 2\kappa R_{ij}^{2}\left(\frac{R_{ij}}{r_{ij}}\right)^{4}\right]$$

$$= \frac{A_{ij}}{r_{ij}^{12}} - \frac{B_{ij}}{r_{ij}^{6}} - \frac{C_{ij}}{r_{ij}^{4}} \tag{3}$$

where C_{ij} is equivalent to $B_{ij}\kappa$, and κ is a parameter in units of $Å^{-2}$ that scales B_{ij}. The additional attractive term, C_{ij}/r_{ij}^{4}, implicitly accounts for polarization effects by mimicking the charge-induced dipole interaction. The C_{ij} value for a divalent metal ion interacting with a nucleic acid site is computed based on the following equation:

$$C_{ij}(\text{ion−nucleic site}) = \frac{C_{ij}(\text{ion−water})}{\alpha(\text{water})} \times \alpha(\text{nucleic site}) \tag{4}$$

where α is an atom type dependent polarizability implemented in AMBER14, with units of $Å^{3}$.

Divalent Ion Model Parametrization for Interaction with RNA. In order to create balanced divalent ion models for interaction with RNA, we depart from the 12−6−4 parameters and tune the value of the pairwise term, C_{ij}, for only the ion−nucleic acid site atom pairs to reproduce the experimental site specific binding free energies.[48] We have computed binding free energies for Mg^{2+}, Mn^{2+}, Zn^{2+}, and Cd^{2+} interacting directly with the N7 of adenosine and guanosine as well as to the nonbridging oxygen of dimethyl phosphate (Figure 1). In this

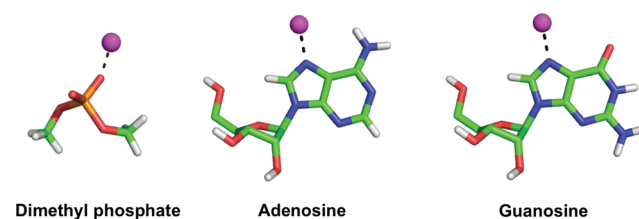**Dimethyl phosphate**   **Adenosine**   **Guanosine**

Figure 1. Model systems and binding sites for which pairwise parameters were tuned in order to reproduce reference experimental binding free energies. The sphere in magenta represents either Mg^{2+}, Mn^{2+}, Zn^{2+}, or Cd^{2+}.

way, our parametrization does not affect the bulk properties of the 12−6−4 ion models, thus leading to ion models that balance both ion−water and ion−RNA interactions. A summary of the 12−6−4 divalent ion models tuned in this study can be found in Table 1. At this time we should note that although experimental affinity data also exist for specific binding to cytidine in ref 48, we do not consider parametrizing to specific sites on cytidine since a recent survey of current structural data indicates the likelihood of inner-sphere binding of Mg^{2+} to cytosine in RNA is very low compared to the other three nucleobases,[53] and there is not an abundance of experimental data available to be confident that the binding affinity is primarily attributed to binding at the O2 atom versus the N3 atom, which is further complicated by data suggesting the dominant binding mode is cation dependent.[54]

The experimental binding free energies for the ion−nucleoside pairs are derived from site specific binding affinities obtained directly from potentiometric pH titration experiments. The reference binding free energies for the ions binding to the phosphodiester bridge, on the other hand, have been estimated

Table 1. Summary of the 12−6−4 Divalent Metal Ion Models, and Their Computed Bulk Properties, That Are Evaluated and Reparametrized in This Study for Use in Nucleic Acid Simulations[a]

ion model	R (Å)	ε (cal/mol)	C_{ij} (Å⁴ kcal/mol)	ΔG[b] (kcal/mol)	R_{ion-O}[b] (Å)	CN_1[c]
Mg^{2+}	1.436	22.37	180.5	-436.3 ± 0.2 (-437.4)	2.08 (2.09 $\pm$ 0.04)	6.0 (6)
Mn^{2+}	1.485	34.50	192.3	-419.5 ± 0.3 (-420.7)	2.18 (2.19 $\pm$ 0.01)	6.7 (6)
Zn^{2+}	1.450	25.45	272.3	-465.4 ± 0.2 (-467.3)	2.08 (2.09 $\pm$ 0.06)	6.0 (6)
Cd^{2+}	1.531	49.54	233.7	-418.5 ± 0.2 (-419.5)	2.29 (2.30 $\pm$ 0.02)	7.8 (6)

[a]The three parameters R, ε, and C_{ij} that describe the 12−6−4 potential functional form can be found in the text. The 12−6−4 divalent ion models were originally parameterized to reproduce ΔG_{solv} (hydration free energy), R_{ion-O} (equilibrium ion−water oxygen distance), and CN (coordination number) and have been computed here for reference. Experimental values are in parentheses. [b]Reference 55. [c]Reference 56.

since stability constants for relevant phosphodiesters have yet to be determined experimentally.[48] Briefly, the stability constants for divalent metal ions binding to phosphodiesters were estimated in three ways: (1) by using the stability constant data previously obtained for acetate and formate, (2) by extrapolating log$K$ versus pK_a plots for phosphate monoesters in the 4.5−8 pK_a range to pK_a = 1, the acidity constant for a phosphate diester, and (3) log$K$ differences between complexes formed with phosphate monoesters and their monoprotonated forms were factored into log$K$ values for phosphate monoesters. Since the computed stability constants obtained from these three approaches were very similar, the log$K$ values were averaged. See Sigel et al. for more details on the estimation of the divalent metal ion−phosphodiester binding free energies.[48]

Calculation of Physical Properties. *Thermodynamics.* Binding free energies for Mg^{2+}, Mn^{2+}, Zn^{2+}, and Cd^{2+} and the nucleic acid sites are computed using thermodynamic integration (TI) via the thermodynamic cycle illustrated in Figure 2. In total, two legs of the thermodynamic cycle are
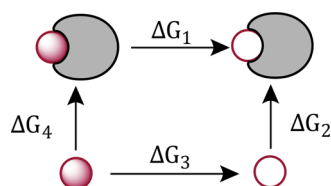

Figure 2. Thermodynamic cycle for computing binding free energies of Mg^{2+}, Mn^{2+}, Zn^{2+}, and Cd^{2+} and specific nucleic acid sites. The filled-in sphere represents a fully interacting divalent metal ion, the hollow sphere represents a noninteracting dummy atom with no charge or LJ parameters, and the gray crescent shape represents the specific nucleic acid sites.

calculated using thermodynamic integration, ΔG_1 and ΔG_3. ΔG_1 is the free energy change for disappearing the ion when it is "bound" to the nucleic acid site while ΔG_3 is the free energy change for disappearing the ion in aqueous solution. For the calculation of ΔG_1, a flat-bottom distance restraint was applied to ensure the ion remained bound to the specific site. The flat-bottom potential was defined with lower and upper bounds of 1.9 and 2.7 Å, respectively, and a 100 kcal/(mol Å²) force constant was employed. The upper bound for the flat bottom restraint was chosen as follows. First, 1 ns long simulations for each of the divalent metal ions bound to the N7 position of adenosine, and restrained by a flat-bottom potential but with lower and upper bounds set to 1.9 and 3.5, respectively, were performed. Subsequently, the distributions of the distances for the four cations were examined, and the tail distance from the Cd^{2+} "bound" distance distribution was chosen as the upper bound for the restraint potential used in all the binding free energy calculations. To directly compare to experiment,

absolute binding free energies (ΔG_b^{comp}) were obtained by including the entropic penalty (ΔG_2) for going from a standard state volume to an allowed "bound" volume defined by the flat-bottom distance restraint:[57,58]

$$\Delta G_2 = -k_B T \left(\frac{\Delta V}{V_{std}} \right) \tag{5}$$

where ΔV is the accessible volume of the divalent metal ion when bound to the nucleic acid site by the flat-bottom distance restraint and V_{std} is the volume accessible to the ion under standard state conditions, or 1661 Å³.[59]

The value for ΔV was obtained by computing the spherical shell volume the ion was restrained to by the flat-bottom potential. Ultimately, ΔG_2 was analytically computed to be 2.0 kcal/mol for all the binding free energy calculations, and the computed absolute binding free energies are derived from the thermodynamic cycle as follows:

$$\Delta G_b^{comp} = -(\Delta G_1 - \Delta G_3) + \Delta G_2 \tag{6}$$

Disappearance of the divalent metal ion in solution (ΔG_3) and bound to the nucleic acid site (ΔG_1) is conducted in three main steps: first, the r^{-4} contribution to the nonbonded potential is removed, followed by the charge, and lastly the Lennard-Jones parameters. The free energy differences for the polarization and charge removing steps are related to the linearly coupled potential energies of the initial and final states, V_0 and V_1, respectively:[60]

$$\Delta G_{TI} = \int_0^1 \left\langle \frac{dV(\lambda)}{d\lambda} \right\rangle_\lambda d\lambda; \quad V(\lambda) = \lambda V_0 + (1-\lambda) V_1 \tag{7}$$

where λ is a coupling parameter that ranges from 0 to 1. By performing simulations at different values of λ, the quantity $\langle dV(\lambda)/d\lambda \rangle_\lambda$ can be directly obtained and the integral in eq 7 can be evaluated to give the free energy difference. In the last step of the thermodynamic integration calculations, however, a nonlinear "softcore" potential is employed for disappearing the Lennard-Jones parameters of the metal ion:[61]

$$V_{softcore} = 4\varepsilon(1-\lambda) \left[\frac{1}{\left[0.5\lambda + 2\left(\frac{r_{ij}}{R_{ij}}\right)^6 \right]^2} - \frac{1}{0.5\lambda + 2\left(\frac{r_{ij}}{R_{ij}}\right)^6} \right] \tag{8}$$

where r_{ij} is the separation distance and R_{ij} is the combined radius for the divalent metal ion and the remaining atoms in the system.

Kinetics. Rates for Mg^{2+}, Mn^{2+}, Zn^{2+}, and Cd^{2+} ions dissociating and associating from dimethyl phosphate; adenosine and guanosine are computed from free energy profiles by applying transition state theory. The activation free energy ($\Delta G^{\ddagger}$) is related to the rate constant (k) as follows:

$$k = A e^{-\Delta G^{\ddagger}/RT} \qquad (9)$$

where A is the pre-exponential factor and is estimated using the second derivative of the energy at the minimum of our free energy profiles and the reduced mass for the nucleic acid site–divalent ion atom pair, $A = (1/2\pi)(E''/\mu)^{1/2}$.

Simulation Protocols. All simulations were performed in the isothermal–isobaric ensemble, and an integration time step of 2 fs was applied. The pressure was maintained by the Berendsen barostat[62] at 1 atm and employing a pressure relaxation time of 1 ps, while the system temperature was kept constant at 298 K by the Langevin[63] thermostat using a 1 ps^{-1} collision frequency. A cutoff of 9 Å was used for nonbonded interactions while long-range electrostatic interactions were treated using the particle mesh Ewald (PME)[64] method. The SHAKE algorithm[65] was used to constrain covalent bonds involving hydrogens. For the divalent ion–nucleic acid model system simulations, a cubic box with 4314 water molecules was utilized. For the hammerhead ribozyme simulations, a rhombo-dodecahedron box with 20 Å clearance between the solute and the edge of the box was used. For more details on the hammerhead ribozyme system setup, see the Supporting Information.

Gas Phase Binding Energy Scans. Gas phase binding energy scans for the four divalent metal ion models and the three nucleic acid sites were performed with AMBER14. Starting structures for the scans were taken from molecular dynamics simulations of the 12−6−4 Mg^{2+} ion bound to dimethyl phosphate and guanosine. Aside from the change in functional groups between guanosine and adenosine, the nucleoside structure used for both residues was identical. Ion–nucleic acid site complexes were then generated with the ion displaced at 0.1 Å intervals from the nucleic acid site along the ion–nucleic acid site atom vector. Both rigid and relaxed gas phase binding energy scans were carried out in the range of 1−9 Å. For the relaxed gas phase curves, 500 cycles of minimization were performed for each ion–nucleic acid site complex with a distance restraint imposed between the ion and binding atom (500 kcal/(mol Å^2) force constant). The final gas phase binding energy scans were obtained by subtracting out the gas phase potential energies of the model nucleic acid systems themselves, $\Delta E_{b} = E_{\text{ion–nucleic acid system}} - E_{\text{nucleic acid system}}$.

Thermodynamic Integration Simulations. Thermodynamic integration simulations[66] were repeated three times to yield the final reported average binding free energies and standard deviations for the four divalent metal ions and the three specific nucleic acid sites. Eleven λ values, evenly spaced at 0.1 unit intervals, were used for all TI simulations. Each λ window was equilibrated for 100 ps, and an additional 1 ns was carried out for use in analysis.

Umbrella Sampling Simulations. Umbrella sampling simulations were used to determine the free energy profiles for the divalent ions dissociating from specific nucleic acid sites. Simulations were started from a 1 ns equilibrated ion–nucleoside/DMP system, where the reaction coordinate was chosen as the distance between the divalent metal ion and either the N7 atom of guanosine/adenosine or one of the nonbridging phosphoryl oxygens of DMP. Umbrella windows

were positioned at 0.1 Å intervals from 2.0 to 6.0 Å, and stepwise equilibration was performed for 20 ps per umbrella window. Each umbrella window was subsequently extended for 10 ns, of which the last 8 ns was ultimately used for analysis.

Umbrella sampling simulations geared toward exploring a metal ion migration hypothesis in the hammerhead ribozyme were started from snapshots taken from two 60 ns MD simulations: one of the ribozyme "reactant" state and the second of the "precursor" state of the reaction (see Supporting Information for details). For each ribozyme state, the four divalent metal ions were pulled from the crystallographic binding site to a second, bridging binding site, and both the 12−6−4 models and the modified 12−6−4 (m12−6−4) models were tested. The reaction coordinate was chosen as a difference in distances between the ion–G10.1:N7 contact breaking in the first binding site and the ion–C17:OP contact forming in the second binding site ($R_1 - R_2$). Stepwise equilibration was conducted for 20 ps for each umbrella window followed by 2 ns production, of which the last 1.5 ns was ultimately used for analysis. Umbrella windows were positioned at 0.1 unit intervals in the range of −3 to 3.

In order to unbias the simulation data and obtain the final free energy profiles, the vFEP[67,68] method was employed and Jacobian corrections were also applied. Finally, convergence was measured for all umbrella sampling simulations as shown in Figures S2, S7, and S8.

■ RESULTS AND DISCUSSION

In the present work, we depart from the 12−6−4 potential models for divalent metal ions recently developed by Li and Merz[24] and tune the pairwise parameters for Mg^{2+}, Mn^{2+}, Zn^{2+}, and Cd^{2+} binding dimethyl phosphate, adenosine, and guanosine in order to reproduce experimental site specific binding free energies derived from potentiometric pH titration data.[48] To this end, we present a series of molecular dynamics simulations that assess the interactions of the Mg^{2+}, Mn^{2+}, Zn^{2+}, and Cd^{2+} 12−6−4 ion models, along with their newly tuned counterparts, denoted as the "m12−6−4" ion models herein, with specific nucleic acid sites via three model systems: dimethyl phosphate (DMP), adenosine (A), and guanosine (G). We further employ the 12−6−4 and m12−6−4 ion parameters to the hammerhead ribozyme, a catalytic RNA system for which a Mg^{2+} ion is believed to play an essential role in catalysis and may change coordination pattern during the reaction. Computed site specific binding free energies, ion–nucleic acid site dissociation free energy profiles, and gas phase ion–nucleic acid site binding energy scans are discussed below.

Divalent Ion–Nucleic Acid Site Absolute Binding Free Energies. The pairwise parameters for the Mg^{2+}, Mn^{2+}, Zn^{2+}, and Cd^{2+} 12−6−4 and m12−6−4 ion models interacting with A:N7, G:N7, and the nonbridging oxygen of dimethyl phosphate, DMP:OP, are summarized in Table 2. R_{ij} and ε_{ij} are the standard Lennard-Jones parameters and represent the combined radius and well depth for a given atom pair. The C_{ij} term mimics the charge-induced dipole interaction and is directly proportional to the polarizability of the atom interacting with the ion (eq 4). In order to reproduce experimental site specific binding free energies, we essentially tune the polarizabilities of the nucleic acid sites (either N7 or OP) until the difference between the computed and experimental binding free energies has been minimized. For reference, the original and final modified polarizabilities are provided in Table S1.

Table 2. Comparison of the Pairwise Parameters for the 12−6−4 and Modified 12−6−4 (m12−6−4) Divalent Ion Models Interacting with the Specific Nucleic Acid Sites[a]

	ion	R_{ij}	ε_{ij}	C_{ij} 12−6−4	C_{ij} m12−6−4
dimethyl phosphate	Mg^{2+}	3.0972	68.53801	71.12500	21.25000
	Mn^{2+}	3.1462	85.11998	75.77472	49.27355
	Zn^{2+}	3.1112	73.11216	107.29827	96.17244
	Cd^{2+}	3.1922	101.99561	92.08816	110.05263
adenosine	Mg^{2+}	3.2600	61.66607	136.25000	238.75000
	Mn^{2+}	3.3090	76.58546	145.15720	235.71399
	Zn^{2+}	3.2740	65.78160	205.54501	279.08864
	Cd^{2+}	3.3550	91.76906	176.40789	255.71053
guanosine	Mg^{2+}	3.2600	61.66607	136.25000	240.62500
	Mn^{2+}	3.3090	76.58546	145.15720	247.69945
	Zn^{2+}	3.2740	65.78160	205.54501	309.26039
	Cd^{2+}	3.3550	91.76906	176.40789	310.73684

[a]The parameters R_{ij}, ε_{ij}, and C_{ij} are described in the text. R_{ij}, ε_{ij}, and C_{ij} have units of Å, cal/mol, and Å[4] kcal/mol, respectively.
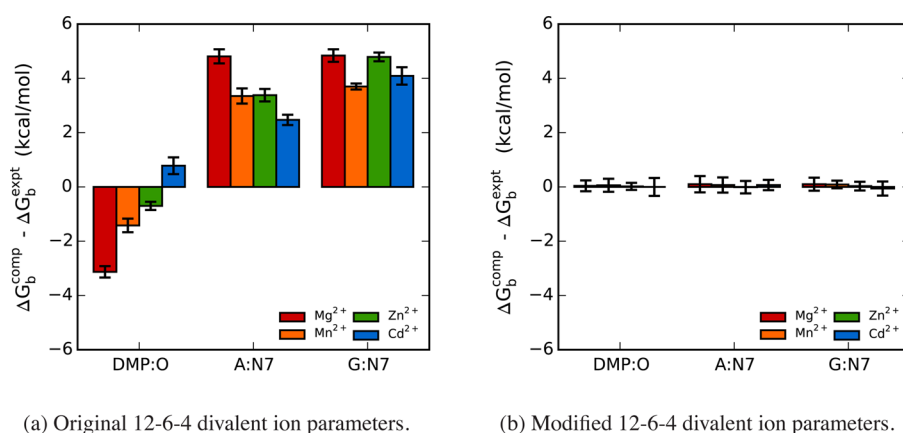
(a) Original 12-6-4 divalent ion parameters.

(b) Modified 12-6-4 divalent ion parameters.

Figure 3. Comparison of error in the absolute binding free energies for the 12−6−4 (left) and m12−6−4 (right) Mg^{2+}, Mn^{2+}, Zn^{2+}, and Cd^{2+} ion parameters and specific nucleic acid sites. The computed values are average binding free energies from three independent simulations, and the errors are estimated from the standard deviations of the three simulations. DMP = dimethyl phosphate, A = adenosine, and G = guanosine.

Figure 3 illustrates a comparison of the error (relative to experiment) in the computed absolute binding free energies for the four divalent metal ions binding to the three nucleic acid sites for the 12−6−4 (a) and m12−6−4 (b) ion models. With the 12−6−4 parameters, the binding free energies for all four ions bound at both A:N7 and G:N7 are underestimated by around 4−5 kcal/mol. The binding free energies for the 12−6−4 ions interacting with DMP:OP, on the other hand, are overestimated for all the ions except Cd^{2+}, which is slightly underestimated. At this point, we should note that we have also evaluated 17 pairwise potential Mg^{2+} ion models (the same set whose bulk properties we previously assessed[47]) in their ability to reproduce the experimental site specific binding free energies at A:N7 and DMP:OP (Figure S1). Our results show that in both cases the 12−6−4 Mg^{2+} models deviate the least from experiment when compared to all the 12−6 potential models. In addition, the direction of the deviation which was observed for the 12−6−4 models (underestimating binding for the nucleosides and overestimating for the phosphodiester group) is preserved when considering the set of 17 Mg^{2+} ion models. The m12−6−4 parameters yield a reduction in error compared to experiment for all the computed binding free energies to 0.1 kcal/mol or less, with estimated standard deviations of 0.3 kcal/mol or less. The absolute binding free energy values from

experiment compared to computed binding free energies for the 12−6−4 and m12−6−4 models are listed in Table S2.

Divalent Ion−Nucleic Acid Site Dissociation Profiles. In an effort to characterize the kinetic behavior of the Mg^{2+}, Mn^{2+}, Zn^{2+}, and Cd^{2+} ion parameters interacting with specific nucleic acid sites, we have obtained the ion-dissociation free energy profiles for both 12−6−4 and m12−6−4 ion models (Figure 4). There are clear differences between the 12−6−4 and m12−6−4 dissociation profiles which correlate with the trends we observed in the computed absolute binding free energies above. Namely, profiles for m12−6−4 ion−nucleic acid interactions whose binding free energies were underestimated with the 12−6−4 parameters are characterized by higher barrier heights while ions whose binding free energies were previously overestimated exhibit lower barriers.

We further extracted several properties from these free energy profiles including transition state distances ($R^{\dagger}$), equilibrium contact distances (R_{min}), pre-exponential factors (A), activation free energies ($\Delta G^{\dagger}$), and rate constants (k) for two processes: ion dissociation and ion association (Table S3). The ratio of the two rate constants for a given ion−nucleic acid site interaction can then be used as a means of comparing the interactions of different ions with the same nucleic acid site. For ion dissociation, the differences in transition state distances and equilibrium contact distances for the 12−6−4 ions versus the
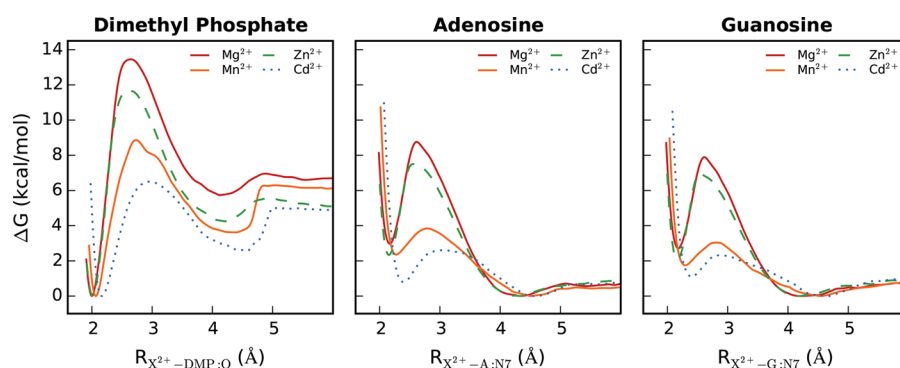
(a) Original 12-6-4 divalent ion parameters.
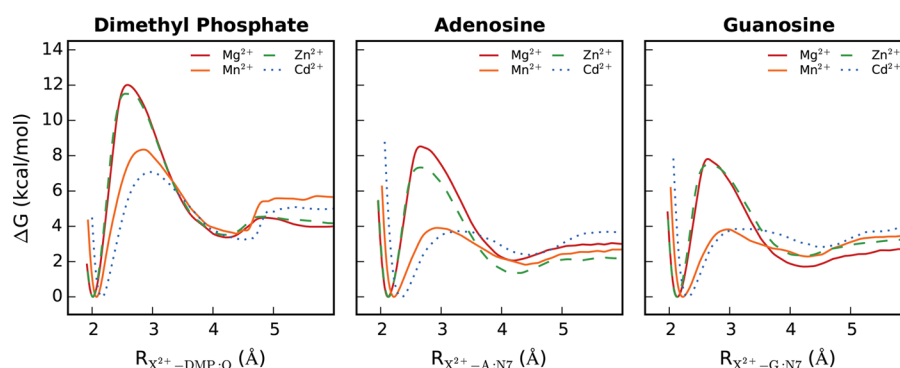
(b) m12-6-4 divalent ion parameters.

Figure 4. Comparison of potential of mean force profiles for the 12−6−4 (top) and m12−6−4 (bottom) Mg^{2+}, Mn^{2+}, Zn^{2+}, and Cd^{2+} ion parameters interacting with specific nucleic acid sites. The profiles depicted here were obtained from the 2 ns segment of umbrella sampling data which yielded a dissociation barrier height closest to the average reported barrier height for each interaction. Left: dimethyl phosphate, middle: adenosine, right: guanosine.

m12−6−4 ions interacting with dimethyl phosphate are for the most part negligible. There are obvious shifts in both of these properties, however, when considering the type of ion parameters interacting with adenosine and guanosine; namely, there is a downward shift in R_{min1} accompanied by an upward shift in $R^{\dagger}$ for the m12−6−4 ion models. There is a similar downward shift in the R_{min-1} values for ion association to these nucleoside sites. Not surprisingly, the barriers for ion association are higher than those for ion dissociation for the 12−6−4 ion−nucleoside interactions, and the corresponding rate ratios are large. This suggests the 12−6−4 ions prefer to be at solvent separation from the N7 position of adenosine and guanosine. The opposite is true for the 12−6−4 ion−dimethyl phosphate interactions. Further, all m12−6−4 ion−nucleic acid interactions maintain global minima at a direct coordinating distance, and ion dissociation barriers are higher than for association in all cases. This can again be correlated, at least qualitatively, to the computed absolute binding free energies. Finally, for any given ion−nucleic acid site interaction (Figure 4), the barrier heights are observed to increase as the ionic radius of the divalent ion model decreases (Table 1).

Reference Gas Phase Metal Ion−Nucleic Acid Site Binding Energy Scans. Gas phase binding energies of divalent ions bound to nucleic acid sites are not necessarily relevant to the binding energetics of these complexes in aqueous solution. Nevertheless, one can extract simple properties from such energy scans like contact distances (σ), minimum energy distances (R), and gas phase binding energies

(ε) that can be used as indexes that may correlate with more complex computed solution phase properties such as equilibrium contact distances and absolute binding free energies. Table 3 summarizes the quantitative data obtained from the rigid binding energy scans for both the 12−6−4 and m12−6−4 ion models interacting with either dimethyl phosphate, adenosine, or guanosine while the adiabatic scans themselves can be found in Figure S3.

In general, the gas phase properties for the 12−6−4 ions versus the m12−6−4 ions interacting with the nucleic acid sites do not change significantly. The contact distances remain nearly identical, and the observed changes in minimum energy distances and binding energies correlate with the computed site specific binding free energies in solution. Thus, for the ion−nucleic acid binding affinities that were underestimated with the 12−6−4 divalent ion parameters in solution, a decrease in the R and ε values is evident from the gas phase binding curves when using the m12−6−4 parameters, and vice versa (Figure S4). Regardless of the parameter set, the gas phase dimethyl phosphate−ion binding curves are characterized by the strongest binding energies and shortest contact and minimum energy distances compared to the nucleoside−metal ion binding curves, with energy differences greater than 100 kcal/mol and distances shorter by about 0.1−0.2 Å. Comparison of the 12−6−4 and m12−6−4 dimethyl phosphate−ion adiabatic curves shows no changes to σ, negligible changes to R, and small changes to ε, with the gas phase binding energies slightly decreasing for Mg^{2+}, Mn^{2+}, and Zn^{2+} (Figures S3 and S4b).

Table 3. Key Features of Nucleic Acid Site−X^{2+} Interaction Energy Scans for the 12−6−4 and m12−6−4 Ion Models[a]

	ion	12−6−4 model			m12−6−4 model		
		σ	R	ε	σ	R	ε
dimethyl phosphate	Mg^{2+}	1.52	1.90	−259.6	1.52	1.91	−255.6
	Mn^{2+}	1.57	1.97	−251.4	1.57	1.97	−249.6
	Zn^{2+}	1.53	1.92	−261.3	1.53	1.92	−260.4
	Cd^{2+}	1.62	2.04	−245.7	1.62	2.03	−246.8
adenosine	Mg^{2+}	1.74	2.06	−61.6	1.72	2.03	−67.5
	Mn^{2+}	1.81	2.14	−57.2	1.79	2.11	−61.7
	Zn^{2+}	1.74	2.06	−68.2	1.73	2.04	−72.4
	Cd^{2+}	1.86	2.20	−56.0	1.85	2.18	−59.5
guanosine	Mg^{2+}	1.70	2.06	−97.2	1.68	2.04	−103.2
	Mn^{2+}	1.76	2.13	−93.0	1.75	2.11	−98.0
	Zn^{2+}	1.70	2.06	−103.4	1.69	2.04	−109.3
	Cd^{2+}	1.81	2.20	−91.6	1.80	2.17	−97.5

[a]"Contact distance" (σ), minimum energy distance (R), and binding energy (ε). Distances and energies are in Å and kcal/mol, respectively.

(a) 12-6-4 metal ion parameters.

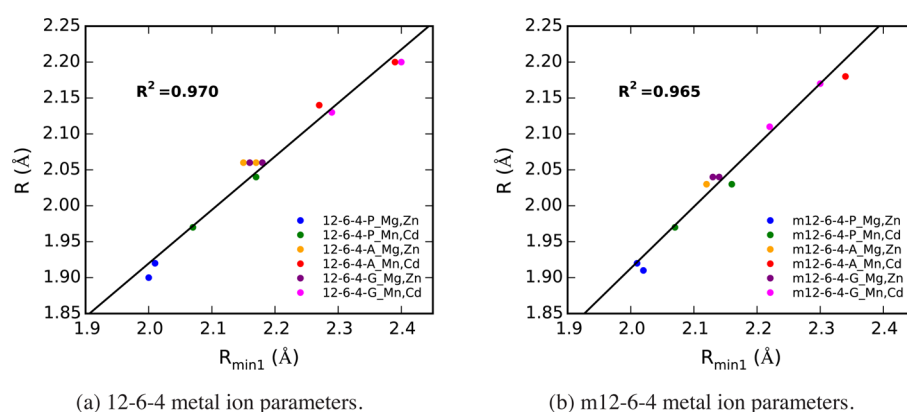(b) m12-6-4 metal ion parameters.

Figure 5. Correlation between gas phase minimum energy distances (R) and computed equilibrium contact distances (R_{min1}) extracted from aqueous solution ion dissociation free energy profiles for the (a) 12−6−4 and (b) m12−6−4 ion models interacting with the three specific nucleic acid sites (P: nonbridging oxygen of dimethyl phosphate; A, G: N7 of adenosine, guanosine). Marker colors distinguish the types of interactions based on not only nucleic acid site but also the identity of the divalent metal ion. The cations are grouped by model ionic radius, with Mg^{2+} and Zn^{2+} making up one group and Mn^{2+} and Cd^{2+} making up another. A line is fit to the data, and the corresponding square of the correlation coefficient, R^2, is shown.

The gas phase binding curves for the divalent metal ions interacting with adenosine and guanosine are characterized by similar contact and minimum energy distances, regardless of parameter type, and yet the ion−guanosine gas phase binding energies are approximately double those for adenosine (Figures S3 and S4a). This is surprising since the solution phase energetics for the ion models interacting with the N7 atom of adenosine versus guanosine, as previously discussed, are at least qualitatively identical and for most interactions even quantitatively similar. In addition, this trend is apparent for both 12−6−4 and m12−6−4 ion−nucleoside curves which suggests that the difference is not related to the different C_{ij} parameters associated with the 12−6−4 and m12−6−4 ion models interacting with the nucleoside N7 atoms (Table 2).

In order to gain further insight into the origin of the differences in ε for the ions binding to guanosine versus adenosine, we have also performed relaxed gas phase energy scans for all metal ion−nucleoside interactions (Figures S5 and S6). For both the ion−adenosine and ion−guanosine gas phase interactions, the ε values from the relaxed scans are more negative. Nevertheless, the ion−adenosine rigid and relaxed scans yield similar trends in the ε values compared to the corresponding ion−guanosine curves (with ε from the relaxed scan almost double the rigid scan ε). This significant decrease in ε for the ion−guanosine relaxed gas phase curves is due to

direct coordination of the ion to both the N7 and O6 guanosine atoms, which does not occur in the rigid scans. We further performed energy decomposition analysis between the metal ions and each atom in the G and A group in order to better understand the energetics of the ion−guanosine and ion−adenosine interactions in the gas phase. Figures S5 and S6 show the electrostatic and van der Waals contributions to the total gas phase binding energies for the 12−6−4 and m12−6−4 parameters, respectively. The large difference in ε values between the ion−adenosine and ion−guanosine curves is shown to be primarily due to differences in the electrostatic energies. A plausible chemical explanation involves the differences in pairwise electrostatic energies for the divalent ion and the O6 atom of guanosine compared to the divalent ion and the exocyclic amine hydrogen belonging to adenosine. Using Mg^{2+} as an example, at the minimum energy distance of the gas phase binding curve, the Mg^{2+}−G:O6 electrostatic energy is equal to −83 kcal/mol while the Mg^{2+}−A:H62 electrostatic energy is 80 kcal/mol. Thus, it is reasonable that the ion−guanosine gas phase binding energy curves are characterized by significantly more favorable ε values, when compared with the ion−adenosine curves.

Additionally, although the trend for the m12−6−4 ion−adenosine and guanosine ε values holds for the corresponding computed absolute binding free energies, e.g., the Mg^{2+}−

adenosine binding energy is less than Mg^{2+}−guanosine binding energy, no such trend is observed for the binding of different ions to a particular nucleic acid site. Further, for all ion−nucleic acid site interactions, there is no linear correlation between the gas phase binding energies and the computed absolute binding free energies (Figure S4). Unlike the binding energies, there is a clear linear correlation between the gas phase minimum energy distances (R) and the equilibrium distances (R_{min1}) extracted from ion dissociation free energy profiles (Figure 5). The square of the correlation coefficient is 0.970 and 0.965 for the 12−6−4 (Figure 5a) and m12−6−4 (Figure 5b) ion models, respectively.

Application of Metal Ion Parameters to the Hammerhead Ribozyme. The hammerhead ribozyme (HHR) is a small self-cleaving ribozyme system found in satellite virus RNAs that has long been used to study RNA enzymology. Crystallographic[69,70] and mutational[71−74] data have implicated G8:O2′ and G12:N1 as the general acid and base in the reaction, respectively, while the role of divalent metal ions in the HHR reaction continues to be disputed. Metal rescue experiments conducted on the minimal HHR system suggested that a Mg^{2+} ion coordinates G10.1:N7 and C17:OP in the ground state of the reaction, while being recruited to a scissile phosphate coordinating position in the reaction transition state.[75] More recently, Cd^{2+} rescue experiments were carried out on the native full-length hammerhead ribozyme with the main result being that the Mg^{2+} ion is coordinating the scissile phosphate in the ground state of the reaction.[76]

In an effort to gain further insight into the role of an active site Mg^{2+} in the full-length hammerhead ribozyme reaction, we previously conducted a molecular dynamics study in which different Mg^{2+} binding sites were probed at different states along the reaction path.[49] The results of these simulations as well as a body of subsequent work[77,78] supported a model where the Mg^{2+}, originally bound at the G10.1/A9 crystallographic binding site, migrated to the scissile phosphate/A9 binding site either in the presence of a deprotonated O2′ nucleophile or in a transition state mimic state of the ribozyme. This so-called metal ion migration, although supported by much of the available experimental data, does not rule out the possibility of an alternative mechanism whereby the metal ion does not change binding sites during the reaction. In the present work, we aim to further explore this metal ion migration model for the hammerhead ribozyme reaction as well as to evaluate the behavior of the 12−6−4 and m12−6−4 ion models when applied to a biologically relevant system where proper modeling of site specific divalent ion−nucleic acid coordination patterns becomes particularly important. To this end, we performed umbrella sampling simulations where the ions were forced to migrate between the crystallographic binding site (C-site) and the scissile phosphate binding site (bridging site) in both the reactant state and activated precursor states of the ribozyme (Figure 6). In the reactant state, all residues are in their physiologically relevant protonation states while the nucleophile O2′ is deprotonated in the activated precursor state of the ribozyme. In total, 16 free energy profiles for metal ion migration (4 cations × 2 ion models × 2 ribozyme states) were obtained (Figure 7).

The key features for the metal ion migration free energy profiles are summarized in Table S6. A clear trend is visible for the free energy barriers associated with going from the C-site to the bridging site (ΔG_1) and vice versa (ΔG_2). For all four divalent metal ions, ΔG_1 decreases by several kcal/mol while
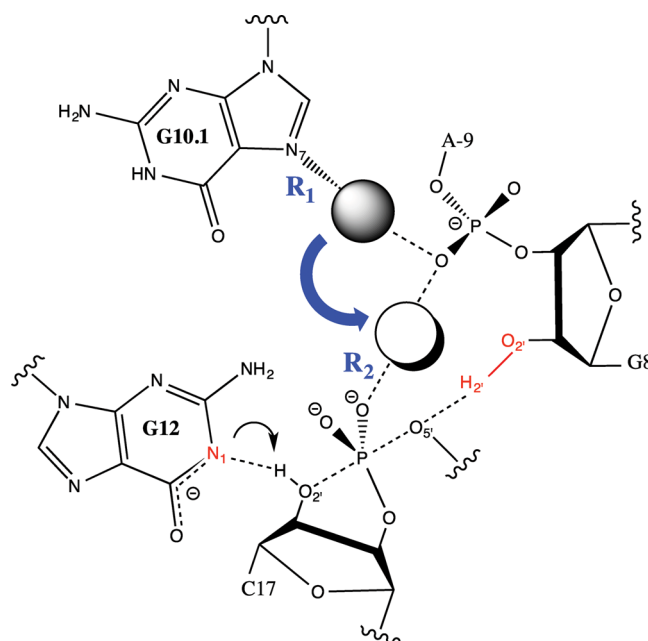

Figure 6. Schematic of the hammerhead ribozyme active site illustrating the previously proposed metal ion migration hypothesis occurring during the catalytic reaction. The reaction coordinate for the metal ion migration free energy profiles conducted was chosen as the difference in the two distances denoted in blue, $R_1 − R_2$, where R_1 is the bond breaking and R_2 is the bond being formed. The general base and acid groups are highlighted in red.

ΔG_2 nearly doubles when in the precursor versus the reactant ribozyme state.

Moreover, the m12−6−4 models exhibit an increased barrier for dissociating from the C-site and a decreased barrier for migrating from the bridging site to the C-site in the reactant state of the reaction. In fact, with the exception of the m12−6−4 Mn^{2+} ion, the free energy at the reaction coordinate value (R_{min1}) corresponding to the C-site is close to zero in the reactant state, which indicates that a divalent metal ion can just as likely be found in the C-site as the bridging site in the HHR reactant state.

The location of the bridging site, as defined by the reaction coordinate (R_{min2}), is also characterized by a shorter C17:OP− ion distance in the precursor state compared to the reactant state. Another key feature of the metal ion migration free energy profiles is the location of the global minimum which for all profiles can be found at a reaction coordinate representing the bridging site.

Comparison of the different metal ion migration energy landscapes for each of the ribozyme states can also provide insight into the behavior of the Mg^{2+}, Mn^{2+}, Zn^{2+}, and Cd^{2+} ions in the catalytic mechanism of the hammerhead ribozyme. Overall, the shapes of the free energy landscapes, for a particular combination of ribozyme state/ion parameters, are similar for Mg^{2+} and Zn^{2+} and also for Mn^{2+} and Cd^{2+}, where the former profiles are clearly characterized by two distinct peaks while the latter profiles show two less defined peaks. In general, we observe that the barrier heights for ΔG_2 for any particular ribozyme state/ion parameter type follow a similar trend across the four metal ions: $Mg^{2+} > Zn^{2+} > Mn^{2+} > Cd^{2+}$. This trend, however, is more pronounced in the HHR precursor state and inversely correlates with the ionic size of the model.
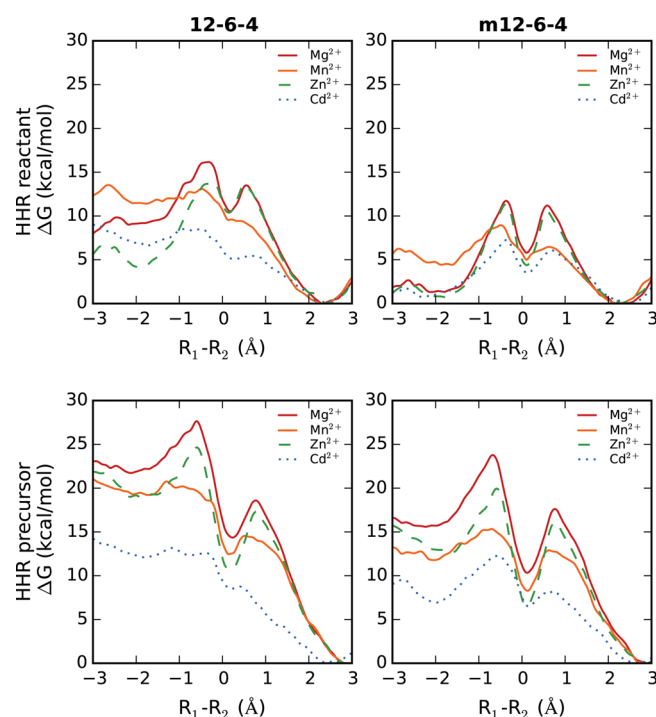
Figure 7. Potential of mean force profiles for the metal ion migration of Mg^{2+}, Mn^{2+}, Zn^{2+}, or Cd^{2+} in either the reactant (top) or activated precursor (bottom) state of the hammerhead ribozyme. Free energy profiles with the original $12-6-4$ ion models (left) and the newly parametrized $m12-6-4$ models (right) are shown. Free energies are in kcal/mol, and the reaction coordinate, $R_1 - R_2$, is defined as the difference in the distances between the ion and G10.1:N7 (R_1) and the ion and C17:OP (R_2). The C-site binding corresponds to the minimum at the negative $R_1 - R_2$ value, and bridging site binding corresponds to the minimum at the positive $R_1 - R_2$ value.

CONCLUSION

In this study, we extended the parametrization of the existing $12-6-4$ Mg^{2+}, Mn^{2+}, Zn^{2+}, and Cd^{2+} ion models to interactions with nucleic acids by tuning pairwise parameters to reproduce experimentally derived binding free energies. Specifically, we targeted direct ion binding at the N7 position of the purines as well as the phosphodiester backbone by using three model systems: adenosine, guanosine, and dimethyl phosphate. The behavior of the $12-6-4$ and the $m12-6-4$ ion models interacting with the nucleic acids sites was evaluated by obtaining adiabatic binding energy curves and ion dissociation free energy profiles. Although no correlation was found between the gas phase binding energies and the computed absolute binding free energies, there was a clear linear correlation between the gas phase minimum energy distances and the solution phase equilibrium distances extracted from ion dissociation free energy profiles. From the ion dissociation free energy profiles, we observed trends for activation free energy barriers consistent with computed site specific binding free energies; i.e., an increase in binding free energy leads to an increase in activation free energy barrier when comparing $12-6-4$ and $m12-6-4$ ion models. Further, the global minimum for all $m12-6-4$ ion–nucleic acid profiles was found to be at a direct coordinating distance, compared to the $12-6-4$ ion–nucleic acid profiles where global minima for the ion–nucleoside interactions were located at a solvent separated distance. After assessing the site specific interactions for both the $12-6-4$ and $m12-6-4$ ion models binding to the three

model systems, we applied both sets of parameters to investigate a possible metal ion migration mechanism in a biologically relevant system: the hammerhead ribozyme. We found that with the newly tuned divalent metal parameters a divalent metal ion (except in the case of Mn^{2+}) is just as likely to reside at the C-site as the bridging site in the reactant state of the ribozyme, although barriers to dissociation from the bridging site in the precursor HHR state are twice as high as those in the reactant state of the ribozyme. In general, barriers to migration from the C-site to the bridging site dropped by several kcal/mol, and barriers to migration from the bridging site to the C-site doubled in the precursor versus the reactant state. Our results illustrate the importance of having accurate and balanced divalent ion parameters for interaction with RNA, especially for applications where a metal ion changes its coordination pattern, and represent a significant step forward in the development of next-generation divalent ion models for molecular simulations of nucleic acid systems.

ASSOCIATED CONTENT

ⓢ Supporting Information

The Supporting Information is available free of charge on the ACS Publications website at DOI: 10.1021/acs.jpcb.5b10423.

> Computed binding free energies for different divalent ion models and nucleic acid sites, nucleic acid site polarizabilities for $12-6-4$ and $m12-6-4$ ion models, convergence criteria for potential of mean force profiles, gas phase ion–nucleic acid binding energy curves, and key features of hammerhead ribozyme metal ion migration free energy profiles (PDF)

AUTHOR INFORMATION

Corresponding Author
*E-mail: Darrin.York@rutgers.edu (D.M.Y.).

Notes
The authors declare no competing financial interest.

ACKNOWLEDGMENTS

REFERENCES

(1) Laederach, A.; Shcherbakova, I.; Jonikas, M. A.; Altman, R. B.; Brenowitz, M. Distinct contribution of electrostatics, initial conformational ensemble, and macromolecular stability in RNA folding. *Proc. Natl. Acad. Sci. U. S. A.* **2007**, *104*, 7045−7050.

(2) Frederiksen, J. K.; Li, N.-S.; Das, R.; Herschlag, D.; Piccirilli, J. A. Metal-ion rescue revisited: Biochemical detection of site-bound metal ions important for RNA folding. *RNA* **2012**, *18*, 1123−1141.

(3) Draper, D. E. A guide to ions and RNA structure. *RNA* **2004**, *10*, 335−343.

(4) Freisinger, E.; Sigel, R. K. O. From nucleotides to ribozymes - A comparison of their metal ion binding properties. *Coord. Chem. Rev.* **2007**, *251*, 1834−1851.

(5) Ferré-D'Amaré, A. R.; Scott, W. G. Small self-cleaving ribozymes. *Cold Spring Harbor Perspect. Biol.* **2010**, *2*, a003574.

(6) Ward, W. L.; Plakos, K.; DeRose, V. J. Nucleic acid catalysis: metals, nucleobases, and other cofactors. *Chem. Rev.* **2014**, *114*, 4318−4342.

(7) Hertweck, M.; Mueller, M. W. Mapping divalent metal ion binding sites in a group II intron by Mn^{2+} and Zn^{2+} induced site-specific RNA cleavage. *Eur. J. Biochem.* **2001**, *268*, 4610−4620.

(8) Wakeman, C. A.; Ramesh, A.; Winkler, W. C. Multiple metal-binding cores are required for metalloregulation by M-box riboswitch RNAs. *J. Mol. Biol.* **2009**, *392*, 723−735.

(9) Ennifar, E.; Walter, P.; Dumas, P. A crystallographic study of the binding of 13 metal ions to two related RNA duplexes. *Nucleic Acids Res.* **2003**, *31*, 2671−2682.

(10) Ramesh, A.; Wakeman, C. A.; Winkler, W. C. Insights into metalloregulation by M-box riboswitch RNAs via structural analysis of manganese-bound complexes. *J. Mol. Biol.* **2011**, *407*, 556−570.

(11) Nakano, S.; Proctor, D. J.; Bevilacqua, P. C. Mechanistic characterization of the HDV genomic ribozyme: Assessing the catalytic and structural contributions of divalent metal ions within a multichannel reaction mechanism. *Biochemistry* **2001**, *40*, 12022−12038.

(12) Shih, I.; Been, M. D. Catalytic strategies of the hepatitis delta virus ribozymes. *Annu. Rev. Biochem.* **2002**, *71*, 887−917.

(13) Lee, T.-S.; Giambaşu, G. M.; Harris, M. E.; York, D. M. Characterization of the structure and dynamics of the HDV ribozyme in different stages along the reaction path. *J. Phys. Chem. Lett.* **2011**, *2*, 2538−2543.

(14) Scott, E. C.; Uhlenbeck, O. C. A re-investigation of the thio effect at the hammerhead cleavage site. *Nucleic Acids Res.* **1999**, *27*, 479−484.

(15) Hougland, J. L.; Kravchuk, A. V.; Herschlag, D.; Piccirilli, J. A. Functional identification of catalytic metal ion binding sites within RNA. *PLoS Biol.* **2005**, *3*, 1536−1548.

(16) Thaplyal, P.; Ganguly, A.; Golden, B. L.; Hammes-Schiffer, S.; Bevilacqua, P. C. Thio effects and an unconventional metal ion rescue in the genomic hepatitis delta virus ribozyme. *Biochemistry* **2013**, *52*, 6499−6514.

(17) Huang, P.; Liu, J. Rational evolution of Cd^{2+}-specific DNAzymes with phosphorothioate modified cleavage junction and Cd^{2+} sensing. *Nucleic Acids Res.* **2015**, *43*, 6125−6133.

(18) Draper, D. E. RNA folding: Thermodynamic and molecular descriptions of the roles of ions. *Biophys. J.* **2008**, *95*, 5489−5495.

(19) Fedor, M. J. Comparative enzymology and structural biology of RNA self-cleavage. *Annu. Rev. Biophys.* **2009**, *38*, 271−299.

(20) Bowman, J. C.; Lenz, T. K.; Hud, N. V.; Williams, L. D. Cations in charge: Magnesium ions in RNA folding and catalysis. *Curr. Opin. Struct. Biol.* **2012**, *22*, 262−272.

(21) Martínez, J. M.; Pappalardo, R. R.; Marcos, E. S. First-principles ion-water interaction potentials for highly charged monatomic cations. Computer simulations of Al^{3+}, Mg^{2+}, and Be^{2+} in water. *J. Am. Chem. Soc.* **1999**, *121*, 3175−3184.

(22) Babu, C. S.; Lim, C. Empirical force fields for biologically active divalent metal cations in water. *J. Phys. Chem. A* **2006**, *110*, 691−699.

(23) Li, P.; Roberts, B. P.; Chakravorty, D. K.; Merz, K. M., Jr. Rational design of Particle Mesh Ewald compatible Lennard-Jones parameters for + 2 metal cations in explicit solvent. *J. Chem. Theory Comput.* **2013**, *9*, 2733−2748.

(24) Li, P.; Merz, K. M., Jr. Taking into account the ion-induced dipole interaction in the nonbonded model of ions. *J. Chem. Theory Comput.* **2014**, *10*, 289−297.

(25) Won, Y. Force field for monovalent, divalent, and trivalent cations developed under the solvent boundary potential. *J. Phys. Chem. A* **2012**, *116*, 11763−11767.

(26) Mayaan, E.; Range, K.; York, D. M. Structure and binding of Mg(II) ions and di-metal bridge complexes with biological phosphates and phosphoranes. *JBIC, J. Biol. Inorg. Chem.* **2004**, *9*, 807−817.

(27) Chaudret, R.; Gresh, N.; Narth, C.; Lagardère, L.; Darden, T. A.; Cisneros, G. A.; Piquemal, J.-P. S/G-1: An ab initio force-field blending frozen hermite gaussian densities and distributed multipoles.

Proof of concept and first applications to metal cations. *J. Phys. Chem. A* **2014**, *118*, 7598−7612.

(28) Tazi, S.; Molina, J. J.; Rotenberg, B.; Turq, P.; Vuilleumier, R.; Salanne, M. A transferable ab initio based force field for aqueous ions. *J. Chem. Phys.* **2012**, *136*, 114507.

(29) Case, D. A.; Berryman, J. T.; Betz, R. M.; Cerutti, D. S.; Cheatham, T. E., III; Darden, T. A.; Duke, R. E.; Giese, T. J.; Gohlke, H.; Goetz, A. W.; et al. *AMBER 15*; University of California, San Francisco, San Francisco, CA, 2015.

(30) Cornell, W. D.; Cieplak, P.; Bayly, C. I.; Gould, I. R.; Merz, K. M., Jr.; Ferguson, D. M.; Spellmeyer, D. C.; Fox, T.; Caldwell, J. W.; Kollman, P. A. A second generation force field for the simulation of proteins, nucleic acids and organic molecules. *J. Am. Chem. Soc.* **1995**, *117*, 5179−5197.

(31) Wang, J.; Cieplak, P.; Kollman, P. A. How well does a restrained electrostatic potential (RESP) model perform in calculating conformational energies of organic biological molecules. *J. Comput. Chem.* **2000**, *21*, 1049−1074.

(32) Pérez, A.; Marchán, I.; Svozil, D.; Sponer, J.; Cheatham, T. E., III; Laughton, C. A.; Orozco, M. Refinement of the AMBER force field for nucleic acids: Improving the description of α/γ conformers. *Biophys. J.* **2007**, *92*, 3817−3829.

(33) Zgarbová, M.; Otyepka, M.; Šponer, J.; Mládek, A.; Banáš, P.; Cheatham, T. E., III; Jurečka, P. Refinement of the Cornell et al. nucleic acids force field based on reference quantum chemical calculations of glycosidic torsion profiles. *J. Chem. Theory Comput.* **2011**, *7*, 2886−2902.

(34) MacKerell, A. D., Jr.; Banavali, N. K. All-atom empirical force field for nucleic acids: II. Application to molecular dynamics simulations of DNA and RNA in solution. *J. Comput. Chem.* **2000**, *21*, 105−120.

(35) Foloppe, N.; MacKerell, A. D., Jr. All-atom empirical force field for nucleic acids: I. Parameter optimization based on small molecule and condensed phase macromolecular target data. *J. Comput. Chem.* **2000**, *21*, 86−104.

(36) Oostenbrink, C.; Villa, A.; Mark, A. E.; van Gunsteren, W. F. A biomolecular force field based on the free enthalpy of hydration and solvation: The GROMOS force-field parameter sets 53A5 and 53A6. *J. Comput. Chem.* **2004**, *25*, 1656−1676.

(37) Jorgensen, W. L.; Maxwell, D. S.; Tirado-Rives, J. Development and testing of the OPLS all-atom force field on conformational energetics and properties of organic liquids. *J. Am. Chem. Soc.* **1996**, *118*, 11225−11236.

(38) Kaminski, G. A.; Friesner, R. A.; Tirado-Rives, J.; Jorgensen, W. L. Evaluation and reparametrization of the OPLS-AA force field for proteins via comparison with accurate quantum chemical calculations on peptides. *J. Phys. Chem. B* **2001**, *105*, 6474−6487.

(39) Ponder, J. W.; Wu, C.; Ren, P.; Pande, V. S.; Chodera, J. D.; Schnieders, M. J.; Haque, I.; Mobley, D. L.; Lambrecht, D. S.; DiStasio, R. A., Jr.; et al. Current status of the AMOEBA polarizable force field. *J. Phys. Chem. B* **2010**, *114*, 2549−2564.

(40) Jiao, D.; King, C.; Grossfield, A.; Darden, T. A.; Ren, P. Simulation of Ca^{2+} and Mg^{2+} solvation using polarizable atomic multipole potential. *J. Phys. Chem. B* **2006**, *110*, 18553−18559.

(41) Grossfield, A.; Ren, P.; Ponder, J. W. Ion solvation thermodynamics from simulation with a polarizable force field. *J. Am. Chem. Soc.* **2003**, *125*, 15671−15682.

(42) Lamoureux, G.; Roux, B. Absolute hydration free energy scale for alkali and halide ions established from simulations with a polarizable force field. *J. Phys. Chem. B* **2006**, *110*, 3308−3322.

(43) Piquemal, J.-P.; Perera, L.; Cisneros, G. A.; Ren, P.; Pedersen, L. G.; Darden, T. A. Towards accurate solvation dynamics of divalent cations in water using the polarizable amoeba force field: From energetics to structure. *J. Chem. Phys.* **2006**, *125*, 054511.

(44) Yu, H.; Whitfield, T. W.; Harder, E.; Lamoureux, G.; Vorobyov, I.; Anisimov, V. M.; MacKerell, A. D., Jr.; Roux, B. Simulating monovalent and divalent ions in aqueous solution using a drude polarizable force field. *J. Chem. Theory Comput.* **2010**, *6*, 774−786.

(45) SpÅngberg, D.; Hermansson, K. Many-body potentials for aqueous Li⁺, Na⁺, Mg²⁺, and Al³⁺: Comparison of effective three-body potentials and polarizable models. *J. Chem. Phys.* **2004**, *120*, 4829−4843.

(46) Duke, R. E.; Starovoytov, O. N.; Piquemal, J.-P.; Cisneros, G. A. GEM*: A molecular electronic density-based force field for molecular dynamics simulations. *J. Chem. Theory Comput.* **2014**, *10*, 1361−1365.

(47) Panteva, M. T.; Giambaşu, G. M.; York, D. M. Comparison of structural, thermodynamic, kinetic and mass transport properties of Mg²⁺ ion models commonly used in biomolecular simulations. *J. Comput. Chem.* **2015**, *36*, 970−982.

(48) Sigel, R. K. O.; Sigel, H. A stability concept for metal ion coordination to single-stranded nucleic acids and affinities of individual sites. *Acc. Chem. Res.* **2010**, *43*, 974−984.

(49) Lee, T.-S.; Silva Lopez, C.; Giambaşu, G. M.; Martick, M.; Scott, W. G.; York, D. M. Role of Mg²⁺ in hammerhead ribozyme catalysis from molecular simulation. *J. Am. Chem. Soc.* **2008**, *130*, 3053−3064.

(50) Horn, H. W.; Swope, W. C.; Pitera, J. W.; Madura, J. D.; Dick, T. J.; Hura, G. L.; Head-Gordon, T. Development of an improved four-site water model for biomolecular simulations: TIP4P-Ew. *J. Chem. Phys.* **2004**, *120*, 9665−9678.

(51) Dupradeau, F.; Pigache, A.; Zaffran, T.; Savineau, C.; Lelong, R.; Grivel, N.; Lelong, D.; Rosanski, W.; Cieplak, P. The R.E.D. tools: Advances in RESP and ESP charge derivation and force field library building. *Phys. Chem. Chem. Phys.* **2010**, *12*, 7821−7839.

(52) Jones, J. E. On the determination of molecular fields. II. From the equation of state of a gas. *Proc. R. Soc. London, Ser. A* **1924**, *106*, 463−477.

(53) Zheng, H.; Shabalin, I. G.; Handing, K. B.; Bujnicki, J. M.; Minor, W. Magnesium-binding architectures in RNA crystal structures: Validation, binding preferences, classification and motif detection. *Nucleic Acids Res.* **2015**, *43*, 3789−3801.

(54) Knobloch, B.; Sigel, H. A quantitative appraisal of the ambivalent metal ion binding properties of cytidine in aqueous solution and an estimation of the anti-syn energy barrier of cytidine derivatives. *JBIC, J. Biol. Inorg. Chem.* **2004**, *9*, 365−373.

(55) Marcus, Y. Thermodynamics of solvation of ions Part 5.-Gibbs free energy of hydration at 298.15 K. *J. Chem. Soc., Faraday Trans.* **1991**, *87*, 2995−2999.

(56) Marcus, Y. Ionic radii in aqueous solutions. *Chem. Rev.* **1988**, *88*, 1475−1498.

(57) Gilson, M. K.; Given, J. A.; Bush, B. L.; McCammon, J. A. The statistical-thermodynamic basis for computation of binding affinities: A critical review. *Biophys. J.* **1997**, *72*, 1047−1069.

(58) Zhou, H.-X.; Gilson, M. K. Theory of free energy and entropy in noncovalent binding. *Chem. Rev.* **2009**, *109*, 4092−4107.

(59) Wang, J.; Deng, Y.; Roux, B. Absolute binding free energy calculations using molecular dynamics simulations with restraining potentials. *Biophys. J.* **2006**, *91*, 2798−2814.

(60) Kirkwood, J. G. Statistical mechanics of fluid mixtures. *J. Chem. Phys.* **1935**, *3*, 300−313.

(61) Steinbrecher, T.; Joung, I.; Case, D. A. Soft-core potentials in thermodynamic integration: Comparing one- and two-step transformations. *J. Comput. Chem.* **2011**, *32*, 3253−3263.

(62) Berendsen, H. J. C.; Postma, J. P. M.; van Gunsteren, W. F.; Dinola, A.; Haak, J. R. Molecular dynamics with coupling to an external bath. *J. Chem. Phys.* **1984**, *81*, 3684−3690.

(63) Turq, P.; Lantelme, F.; Friedman, H. L. Brownian dynamics: Its application to ionic solutions. *J. Chem. Phys.* **1977**, *66*, 3039−3044.

(64) Darden, T.; York, D.; Pedersen, L. Particle mesh Ewald: An N log(N) method for Ewald sums in large systems. *J. Chem. Phys.* **1993**, *98*, 10089−10092.

(65) Ryckaert, J. P.; Ciccotti, G.; Berendsen, H. J. C. Numerical integration of the cartesian equations of motion of a system with constraints: Molecular dynamics of n-alkanes. *J. Comput. Phys.* **1977**, *23*, 327−341.

(66) Kaus, J. W.; Pierce, L. T.; Walker, R. C.; McCammon, J. A. Improving the efficiency of free energy calculations in the Amber molecular dynamics package. *J. Chem. Theory Comput.* **2013**, *9*, 4131−4139.

(67) Lee, T.-S.; Radak, B. K.; Pabis, A.; York, D. M. A new maximum likelihood approach for free energy profile construction from molecular simulations. *J. Chem. Theory Comput.* **2013**, *9*, 153−164.

(68) Lee, T.-S.; Radak, B. K.; Huang, M.; Wong, K.-Y.; York, D. M. Roadmaps through free energy landscapes calculated using the multidimensional vFEP approach. *J. Chem. Theory Comput.* **2014**, *10*, 24−34.

(69) Wedekind, J. E.; McKay, D. B. Crystallographic structures of the hammerhead ribozyme: Relationship to ribozyme folding and catalysis. *Annu. Rev. Biophys. Biomol. Struct.* **1998**, *27*, 475−502.

(70) Martick, M.; Lee, T.-S.; York, D. M.; Scott, W. G. Solvent structure and hammerhead ribozyme catalysis. *Chem. Biol.* **2008**, *15*, 332−342.

(71) Blount, K. F.; Uhlenbeck, O. C. The structure-function dilemma of the hammerhead ribozyme. *Annu. Rev. Biophys. Biomol. Struct.* **2005**, *34*, 415−440.

(72) Han, J.; Burke, J. M. Model for general acid-base catalysis by the hammerhead ribozyme: pH-activity relationships of G8 and G12 variants at the putative active site. *Biochemistry* **2005**, *44*, 7864−7870.

(73) Grasby, J. A.; Mersmann, K.; Singh, M.; Gait, M. J. Purine functional groups in essential residues of the hairpin ribozyme required for catalytic cleavage of RNA. *Biochemistry* **1995**, *34*, 4068−4076.

(74) Chi, Y.-I.; Martick, M.; Lares, M.; Kim, R.; Scott, W. G.; Kim, S.-H. Capturing hammerhead ribozyme structures in action by modulating general base catalysis. *PLoS Biol.* **2008**, *6*, e234.

(75) Wang, S.; Karbstein, K.; Peracchi, A.; Beigelman, L.; Herschlag, D. Identification of the hammerhead ribozyme metal ion binding site responsible for rescue of the deleterious effect of a cleavage site phosphorothioate. *Biochemistry* **1999**, *38*, 14363−14378.

(76) Ward, W. L.; Derose, V. J. Ground-state coordination of a catalytic metal to the scissile phosphate of a tertiary-stabilized hammerhead ribozyme. *RNA* **2012**, *18*, 16−23.

(77) Wong, K.-Y.; Lee, T.-S.; York, D. M. Active participation of the Mg²⁺ ion in the reaction coordinate of RNA self-cleavage catalyzed by the hammerhead ribozyme. *J. Chem. Theory Comput.* **2011**, *7*, 1−3.

(78) Lee, T.-S.; Wong, K.-Y.; Giambaşu, G. M.; York, D. M. In *Progress in Molecular Biology and Translational Science*; Soukup, G. A., Ed.; Academic Press: Oxford, UK, 2013; Vol. *120*, pp 25−91.